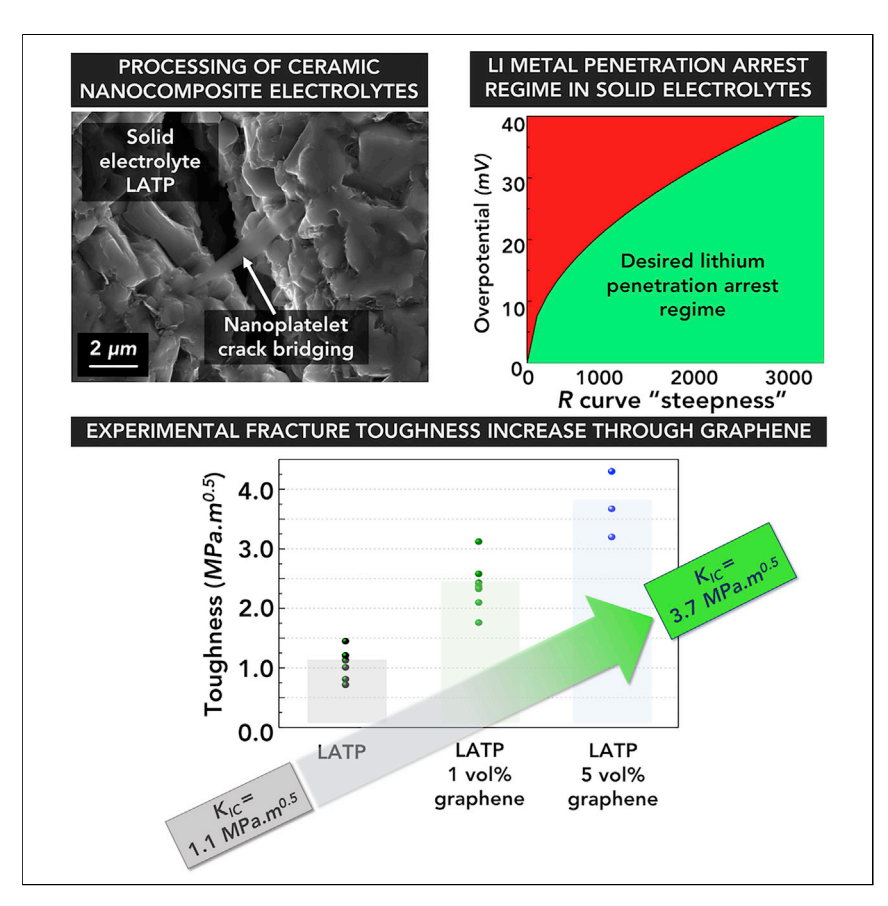
# **Matter**



## **Article**

# High-Toughness Inorganic Solid Electrolytes via the Use of Reduced Graphene Oxide



Solid-state lithium batteries can increase the energy density of lithium-ion batteries by enabling the safe ("lithium metal penetration free") use of lithium-metal anodes. In this work, we show that toughened ceramic electrolytes can be designed via the use of nanomaterials such as reduced graphene oxide. This increased toughness offers a viable way to inhibit short-circuits due to lithium-metal penetration.

Christos E. Athanasiou, Mok Yun Jin, Cristina Ramirez, Nitin P. Padture, Brian W. Sheldon

christos\_edouardos\_athanasiou@brown. edu (C.E.A.) brian\_sheldon@brown.edu (B.W.S.)

#### **HIGHLIGHTS**

Over two-fold toughness enhancement in LATP ceramic electrolytes is demonstrated

Increased toughness does not alter the ionic and electronic behavior of the material

A framework is developed for designing tough solid electrolytes using 2D materials

Demonstrate
Proof-of-concept of performance with intended application/response

Athanasiou et al., Matter 3, 212–229 July 1, 2020 © 2020 The Authors. Published by Elsevier Inc.

https://doi.org/10.1016/j.matt.2020.05.003







## **Article**

## High-Toughness Inorganic Solid Electrolytes via the Use of Reduced Graphene Oxide

Christos E. Athanasiou, 1,\* Mok Yun Jin, 1 Cristina Ramirez, 1 Nitin P. Padture, 1 and Brian W. Sheldon 1,2,\*

## **SUMMARY**

Ceramic solid electrolytes are important emerging materials with the potential to enable the safe use of Li-metal anodes. However, they suffer from inherently low fracture toughness, which significantly limits battery performance and reliability. While small electrolyte dimensions are generally needed for faster ion transport, these length scales also restrict the approaches that can be used to engineer higher fracture resistance. Inspired by the toughening that reduced graphene oxide provides to polymers and engineering ceramics, this study explores the use of rGO to enhance the toughness of an oxide-based lithiumion conductor. Materials with a greater than 2-fold enhancement in the average  $K_{\rm IC}$  are demonstrated. To our knowledge, this is the toughest ceramic solid electrolyte yet reported. Based on these results, an analytical framework is developed to provide guidelines for the design of ultra-tough solid electrolytes using 2D materials.

## INTRODUCTION

Solid-state lithium batteries (SSLBs) provide key improvements to traditional lithium (Li)-ion batteries based on liquid electrolytes. They can potentially increase energy density through the safe use of Li-metal anodes.<sup>2-4</sup> Solid-state electrolytes (SSEs) are the enabling material for the successful development of SSLBs. 5,6 However, ceramic solid electrolytes still suffer from challenges related to their mechanical properties. In particular, the low fracture toughness ( $K_{IC}$ ) of these materials (~1 MPa.m<sup>0.5</sup>) is a major limitation.<sup>2,3,7</sup> Limited attempts to increase the fracture toughness of these electrolytes have not been successful, as high ionic conductivity together with increased  $K_{IC}$  was not achieved. <sup>8,9</sup> Nanoscale reinforcements such as nanoparticles, carbon nanotubes, and graphene-related platelets have been used to increase the toughness of structural ceramics, with multiple studies showing that low volume fractions (1-5 vol %) of reduced graphene oxide (rGO) are particularly successful. 10-14 These strategies have not been explored in solid electrolytes. Thus, rGO was selected to reinforce ceramic electrolytes in the current work. This was incorporated in Li<sub>1+x</sub>Al<sub>x</sub>Ti<sub>2-x</sub>(PO<sub>4</sub>)<sub>3</sub> (LATP), which is an easy-to-fabricate, lowcost NaSICON-type inorganic electrolyte with high stability in air and/or water. 15 Spark plasma sintering (SPS) is widely used to fabricate ceramic nanocomposites, largely because high heating rates make it possible to obtain dense material with very small grain sizes. 11-14 Prior research shows that SPS can produce LATP with high ionic conductivity ( $\sim 10^{-3}$  S cm<sup>-1</sup>),  $^{16,17}$  and this method was extended to produce LATP/rGO nanocomposites. The microstructure, fracture toughness and conductivity of these nanocomposites is reported here. Fracture of SSEs in Li-ion batteries is then discussed, along with their potential for limiting the propagation of Li-metal dendrites.

## **Progress and Potential**

Ceramic electrolytes are a promising replacement for the liquid electrolytes that are commonly used in Li-ion batteries. The implementation of solid electrolytes can potentially lead to both higher energy density and improved safety. However, their inherently low fracture toughness is a major limitation. In this work, a method to fabricate hightoughness ceramic solid electrolytes is proposed and demonstrated. These nanocomposite materials use low volume fractions of reduced graphene oxide, and show over two-fold increase in the fracture toughness in LATP with negligible change in ionic and electrical conductivities. An overall framework is also presented to assess the relevant toughening length scales and to provide guidelines for designing toughened solid electrolytes using nanomaterials.







Table 1. Effect of Temperature on the LATP Microstructure

| Processing Measurements | Temperature (°C) |              |               |
|-------------------------|------------------|--------------|---------------|
|                         | 800              | 850          | 950           |
| Average grain size (μm) | 1.8 ± 0.1        | 2.1 ± 0.1    | $2.5 \pm 0.1$ |
| Relative density (%)    | 81.12 ± 0.05     | 87.75 ± 0.05 | 91.38 ± 0.05  |

## **RESULTS AND DISCUSSION**

## **LATP Nanocomposite Structural and Mechanical Investigation**

Research on ceramic nanocomposites is notoriously challenging, with numerous studies that show poor mechanical properties due to inhomogeneous microstructures. 18 For this reason, SPS was employed to demonstrate the feasibility of creating nanocomposite electrolytes. This method allows full-density processing quickly, avoiding degradation of the rGO reinforcements. SPS also makes it possible to maintain nanostructured composite materials, in contrast to conventional sintering methods, whereby much higher temperatures lead to substantial grain growth. Three different processing temperatures were evaluated for LATP (as illustrated in Table 1). The sintering conditions were based on prior SPS studies for this material. 16,17 Scanning electron microscopy (SEM) shows that higher temperature and/or longer sintering times promote densification but also enhance grain growth. The effect of temperature is evident in Table 1 and Figure 1. It is clear that fully dense material is not achieved at 800°C. However, higher relative density (91.4%) was observed at 950°C, along with substantial grain growth (2.5 μm). With these conditions, the relative density for LATP with 1 and 5 vol % rGO was similar (91.0% and 90.7%, respectively). Retained porosity is expected to degrade the performance of the material (both electrochemically and mechanically). 19-21 The impact of grain size on electrochemical properties is unclear. The rGO platelet thickness and lateral dimensions are 60-120 nm and 5-10  $\mu$ m.

Structural characterization of the LATP was conducted using X-ray diffraction (XRD). The main peaks in all patterns were indexed to the Li<sub>1,3</sub>Al<sub>0,3</sub>Ti<sub>1,7</sub>(PO<sub>4</sub>)<sub>3</sub> crystal structure (Joint Commission on Powder Diffraction Standards card 35-0754), as shown in Figure 2A. Evidence of a small amount of AIPO<sub>4</sub> was detected in all the sintered materials. With the addition of GO, some peaks are enhanced. For the 5 vol % composite the additional peak at  $\sim$ 31.3 $^{\circ}$  (not present in the starting powder) may be due to  $\text{Li}_2\text{C}_2$ . Further structural characterization of the composites was conducted using Raman spectroscopy (Figure 2B). The characteristic D and G bands for graphitic structures were observed, as well as the peak that corresponds to  $PO_4^{3-}$ . The G band is a fundamental frequency of graphitic structures. The weak presence of the two-dimensional (2D) band for the case of LATP with 5% rGO indicates successful thermal reduction of GO to rGO. 11,12

Standard methods (described in Experimental Procedures) were employed to measure the fracture toughness of the monolithic material (LATP) and the composites. To determine the fracture toughness of monolithic LATP, we first evaluated the elastic modulus (102.5 GPa) and hardness (8.0 GPa) with nanoindentation. These values are consistent with other reported values for LATP produced with SPS. 7,16,17 The elastic modulus of the composite nanocomposite decreased with the addition of rGO. For the nanocomposites, the measured elastic modulus values are 97.7 and 81.6 GPa with 1% and 5%, rGO respectively. The measured toughness for both the monolithic and composite materials are reported in Figure 3. It is important to note that indentation methods are not capable of providing accurate quantitative information about

<sup>&</sup>lt;sup>1</sup>School of Engineering, Brown University, Providence, RI 02912, USA

<sup>&</sup>lt;sup>2</sup>Lead Contact

<sup>\*</sup>Correspondence:

christos\_edouardos\_athanasiou@brown.edu (C.E.A.), brian\_sheldon@brown.edu (B.W.S.) https://doi.org/10.1016/j.matt.2020.05.003





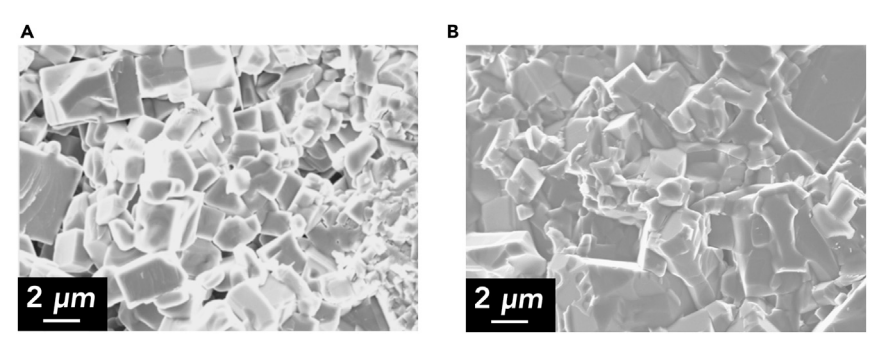


Figure 1. Sintered LATP Ceramic Electrolyte Microscope Images

(A) SEM images of fracture surfaces of LATP ceramic electrolytes densified under different SPS conditions. The uneven grain growth and porosity observed indicate that sintering at 800°C is insufficient to achieve fully dense material.

(B) Grain growth accompanied by some porosity removal occurs after annealing at 950°C.

the toughness in nanocomposites,  $^{24,25}$  and thus the values reported here were obtained with traditional large-scale measurements. The mean toughness value,  $K_{\rm lc}^{\rm avg}$ , for LATP is 1.1 MPa.m<sup>0.5</sup>, the value for the 1 vol % composite increases to 2.4 MPa.m<sup>0.5</sup>, and the value for the 5 vol % composite increases substantially to 3.7 MPa.m<sup>0.5</sup>. The increased fracture toughness in the composites is believed to be primarily caused by crack deflection followed by bridging and pull-out of the rGO platelets, as shown in Figure 4A. The properties of the platelet/matrix interface are known to be critically important here. Crack deflection generally requires a sufficiently weak interface, and energy dissipation due to debonding and frictional sliding along this interface, leads to increased toughness. 11,12

To confirm the occurrence of bridging in the rGO-reinforced LATP, we used SEM to examine indentation cracks (Figure 4B). Crack deflection (Figure 4C), rGO bridging (Figures 4D and 4E), and pull-out (Figures 4F and 4G) are all evident. These qualitative observations, along with the measured increase in toughness, indicate that LATP can be reinforced successfully with low rGO volume fractions.

## **LATP Nanocomposite Electrochemical Performance**

In addition to demonstrating improved mechanical behavior in the LATP/rGO composites, it is also necessary to determine whether these materials meet the conductivity requirements of a functional electrolyte. These properties, reported in Figure 5A, show that the ionic conductivity is on the order of  $10^{-5}$  S.cm<sup>-1</sup> for both the LATP and LATP/1 vol % rGO composite. These values are similar to other reported values for SPS'd LATP with similar thicknesses. <sup>16,17</sup> The electronic conductivities of  $\sim 0.5 \times 10^{-8}$  S.cm<sup>-1</sup> are also similar others reported. This demonstrates that a low volume percentage of rGO (1 vol %) increases the fracture toughness without significantly altering the ionic and electronic conductivities of the solid electrolyte. For higher volume percentages (i.e., LATP/5 vol % rGO), the increase in the electronic conductivity is probably due to the creation of a percolating conductive carbon network across the material. While this composite cannot be used as an electrolyte, it is likely that much lower electrical conductivity with these higher reinforcement volume fractions can be achieved with additional modifications (e.g., by coating the rGO with a thin film insulator).

To further increase the ionic conductivity, we annealed specimens at 950°C for 10 h in forming gas (5% hydrogen and 95% nitrogen). A modest annealing temperature value was chosen to minimize the impact of grain growth on the mechanical



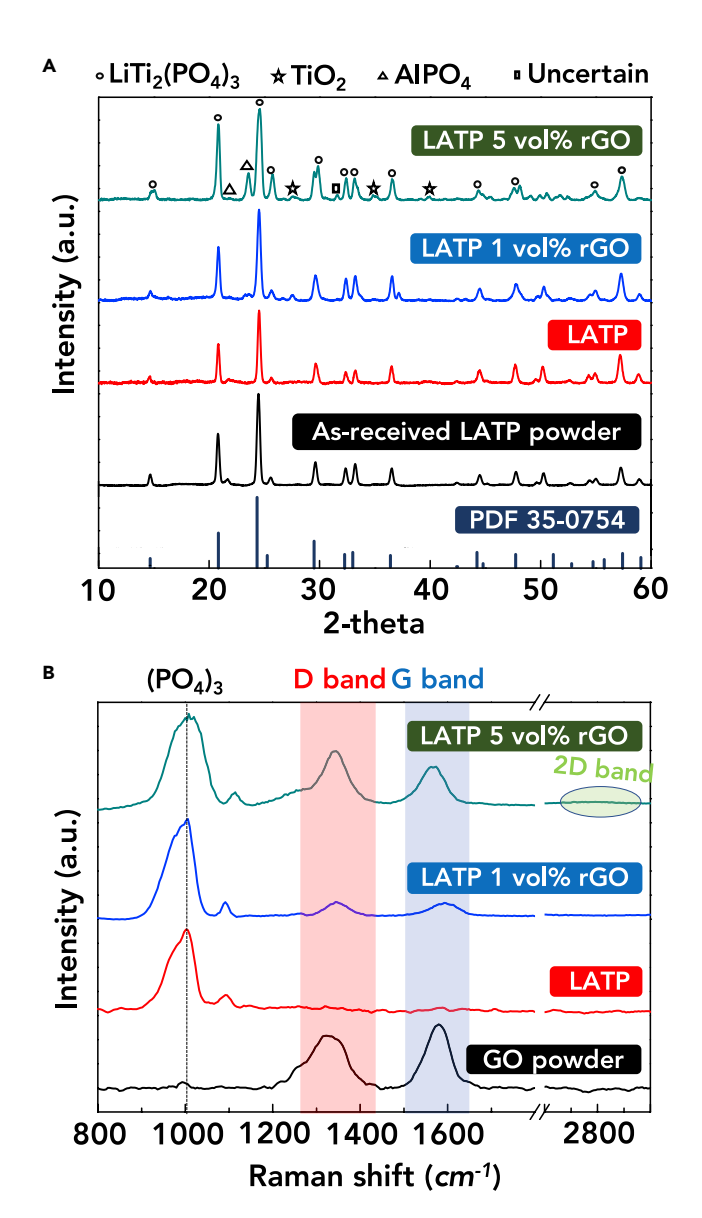


Figure 2. Structural Characterization of LATP/rGO Nanocomposites

(A) XRD of the prepared  $Li_{1.3}Al_{0.3}Ti_{1.7}(PO_4)_3$  for as-received powder (black), SPS'd monolithic LATP materials (red), LATP with the addition of 1 vol % rGO (blue), and LATP with the addition of 5 vol %rGO (green). Some of the peaks are suppressed when graphene oxide is added. Reference lines for LATP are also shown (dark blue).

(B) Raman spectra of the GO powder (black), SPS'd monolithic LATP materials (red), LATP with the addition of 1 vol % rGO (blue), and LATP with the addition of 5 vol % rGO (green). The presence of the 2D band in the LATP 5 vol % composite indicates successful reduction of the GO to rGO after SPS sintering.

properties. As seen in Figure 5A, this led to some increase in ionic conductivity. Although ionic conductivity mechanisms are still not widely understood, there are several reports of grain-boundary conductivity being well below bulk conductivity.<sup>26,27</sup> Based on this, one possible explanation for the higher conductivity is that oxidation at higher temperatures or for longer times may increase the grain size. In general, further improvements in the conductivities of the LATP/rGO composites are desirable. Other work with ceramic solid electrolytes demonstrates that process





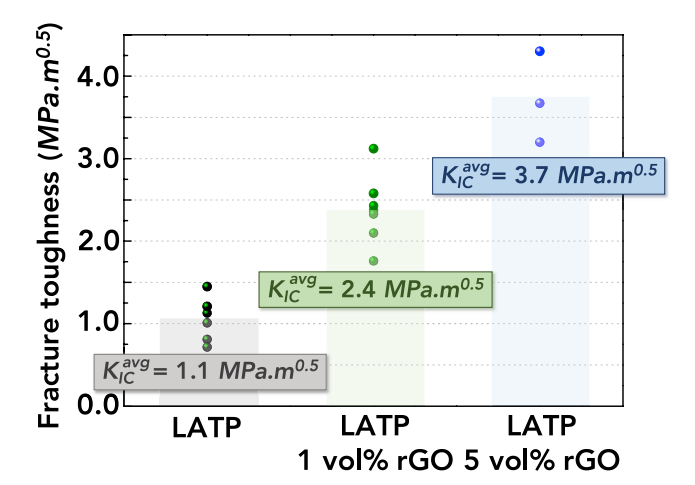


Figure 3. Fracture Toughness Enhancements

Fracture toughness of monolithic and rGO-reinforced LATP, obtained by Vickers indentation and single-edge-notched beam tests, respectively.  $K_{\rm IC}^{\rm avg}$  is the average fracture toughness for each type of material.

optimization studies can be used to obtain additional improvements in the ionic conductivity values, and similar results are likely to be possible with the LATP/rGO nanocomposites. <sup>28,29</sup>

To evaluate the electrochemical cycling behavior of the composite electrolyte, we performed experiments using symmetric coin cells (Figure 5B). In general, oxide solid electrolytes are not thermodynamically stable against Li metal.  $^{30-32}$  The mechanisms associated with the corresponding decomposition and passivation of these materials are currently not well understood. One key problem for Ti-based systems is the reduction of Ti $^{4+}$  to Ti $^{3+}$  in the presence of metallic Li.  $^{30-32}$  Other work indicates that better performance can be achieved when LATP surfaces are stabilized with surface coatings, such as Li $_2\text{PO}_2\text{N}^{26,33}$  or poly(ethylene oxide) (PEO).  $^{34}$  Based on this, a thin PEO layer was employed to demonstrate the feasibility of this approach with the LATP nanocomposites. Results obtained with the oxidized LATP composite at a current density of 0.01 mA cm $^{-2}$  are shown in Figure 5C. After several cycles the results indicate that the overpotential does not increase, and the impedance spectra in Figure 5D confirm that the interfacial resistance of the LATP composite does not increase during cycling.

## **Analysis of Nanocomposite Fracture**

The measurements in Figure 3 demonstrate that low volume fractions of rGO lead to significant toughening. However, it is important to look beyond  $K_{\rm lc}$  values to address relevant phenomena at the length scales that are relevant in solid electrolytes. In particular, describing nanocomposite fracture with  $K_{\rm lc}$  is incomplete because of large-scale bridging (LSB).<sup>35</sup> These effects are expected to lead to the type of R-curve behavior that is shown schematically in Figure 6. The fracture resistance for the matrix,  $R^{\circ}$ , corresponds to the  $K_{\rm lc}^{\circ}$  value, via

$$R^{\circ} = \frac{K_{lc}^{\circ 2}}{E_{E}'},$$
 (Equation 1)

where the plane strain modulus,  $E_E' = E_E/(1 - v_E^2)$ , is a function of the elastic modulus,  $E_E$ , and the Poisson ratio,  $v_E$ .





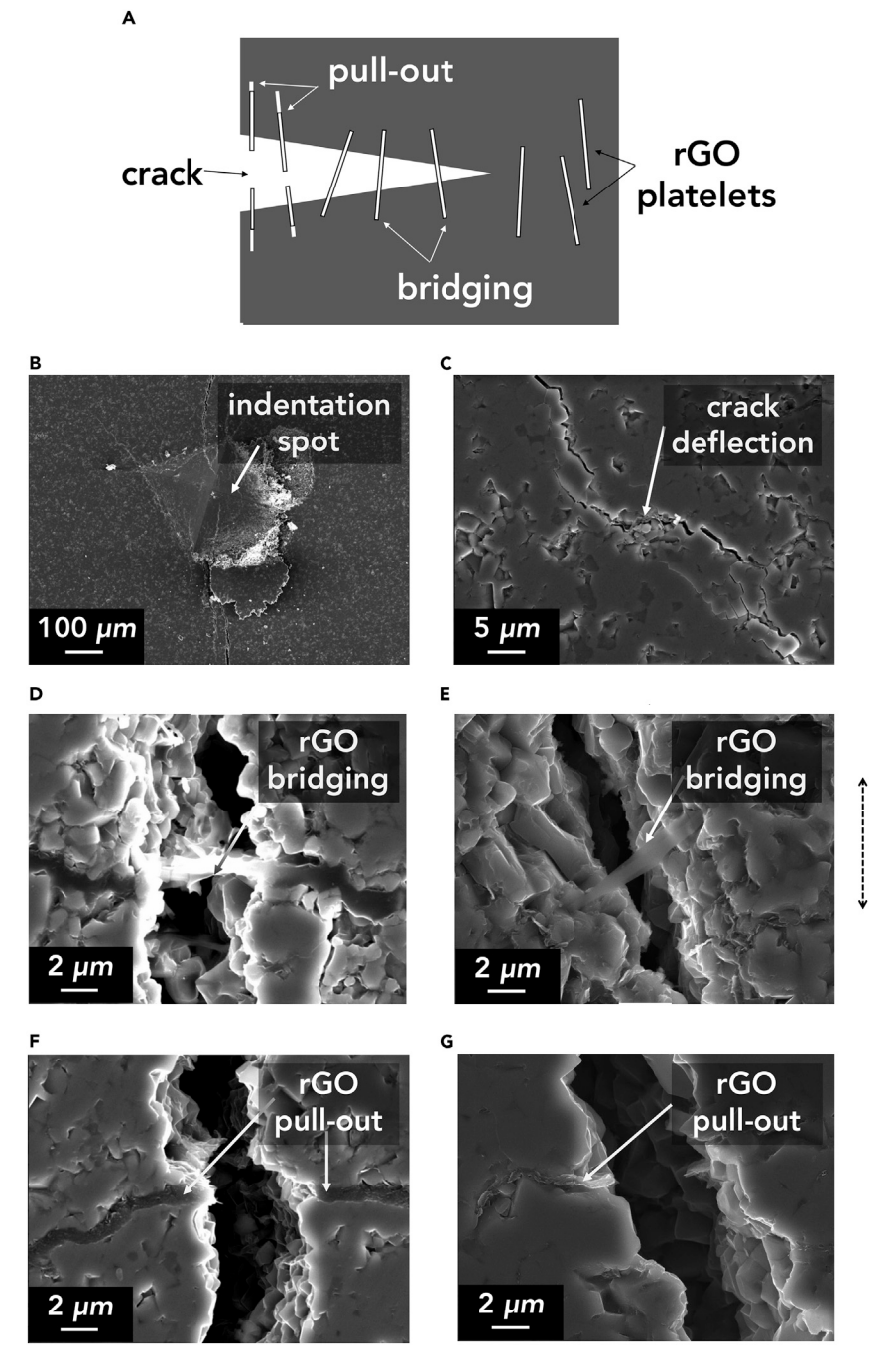


Figure 4. Fracture Toughness Enhancements via Crack Deflection and rGO Pull-Out (A) Simplified schematic of crack bridging and pull-out. SEM images of: (B) the indentation spot, (C) crack deflection near indent, (D and E) crack bridging by an rGO platelet, and (F and G) evidence of rGO platelet pull-out. The dashed double arrow indicates the direction of the mechanical pressure applied during SPS sintering.

Crack extension occurs when G > R, where G is the strain energy-release rate. In general G is determined by the specimen geometry (including the crack length, c). For basic mode I loading (uniaxial tension), G increases with c and with the applied load. For a single-phase ceramic (i.e., the LATP matrix) this leads to unstable crack



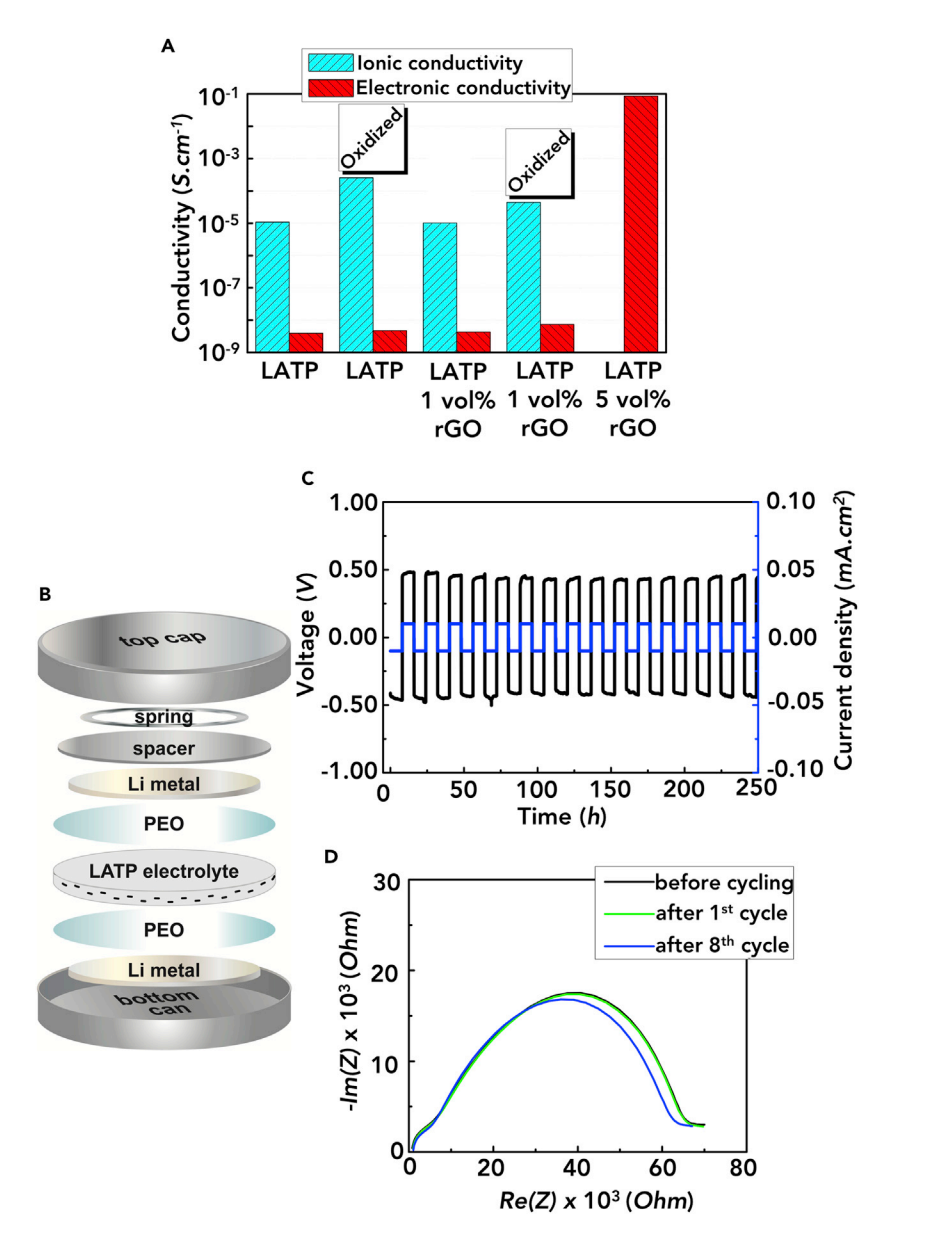


Figure 5. Electrochemical Performance of LATP/rGO Nanocomposites

- (A) Ionic and electronic conductivity of monolithic and composite materials.
- (B) Schematic of the symmetric cell with Li-metal electrodes and PEO passivation layers.
- (C) Voltage profile of the oxidized LATP composite for cycling at 0.01 mA  $\rm cm^{-2}$ .
- (D) Electrochemical impedance spectra confirm that the impedance does not increase.

extension (i.e., G>R is satisfied for all  $c>c_0$ ). This case is shown as the dotted line beyond the  $G^\circ=R^\circ$  value in Figure 6B.

The rGO reinforcements lead to additional toughening above the  $R^{\circ}$  value. In Figure 6B this increase in R extends across most of the electrolyte thickness. This depiction is based on recent measurements with similar rGO reinforcements in a different ceramic matrix (SPS-processed Al $_2$ O $_3$ ), which show that steady-state bridging-zone sizes are on the order of 100  $\mu m.^{11}$  Similar behavior in the LATP nanocomposites was verified with SEM observations which show an average of  $\sim\!\!28$  and  $\sim\!\!8$  bridging platelets per 100  $\mu m$  of crack length in the 5 vol % and



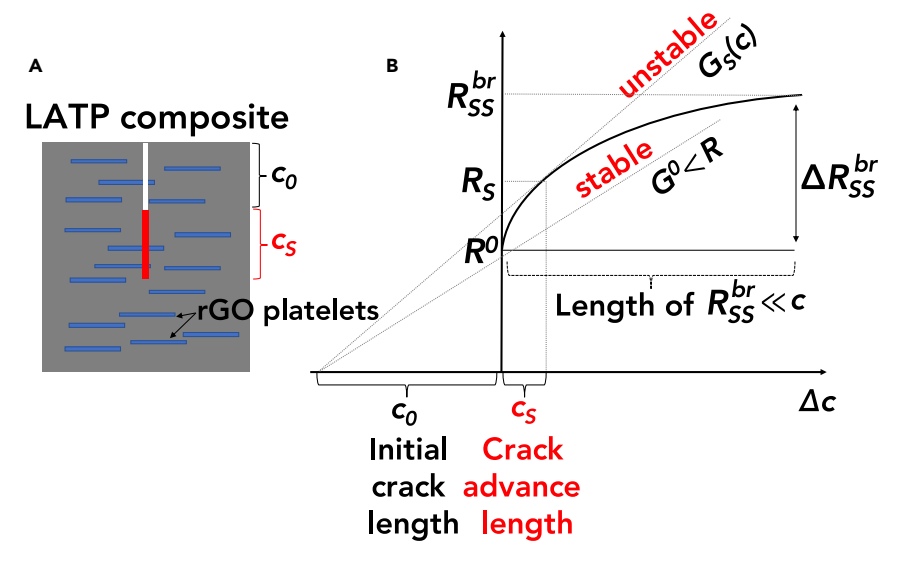


Figure 6. Analysis of Nanocomposite Fracture

(A) Schematic of a nanocomposite solid electrolyte with initial crack length ( $c_o$ ) and crack extension ( $c_s$ ).

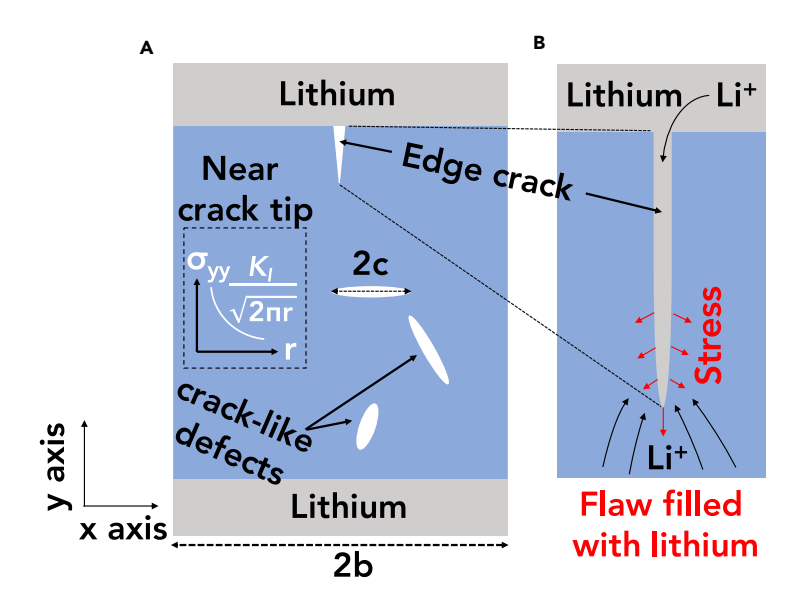
(B) Schematic of rising fracture resistance (i.e., R curve) and strain energy release rate, G, for external mode I loading.

1 vol % nanocomposites, respectively. Estimates for the number of vertically aligned, randomly distributed platelets in the cross-section of a rectangular volume are 32 and 6 platelets along a 100- $\mu m$  crack for 5 vol % and 1 vol % loadings (based on rGO dimensions of 100-nm thickness and a radius of 10  $\mu m$ ).  $^{36}$  The similarity between these values and the SEM observations demonstrates that the rGO platelets in the LATP nanocomposites are well dispersed and aligned. Based on these findings, the bridging zone in these materials is expected to evolve during crack extension over at least tens of micrometers. Further investigations of bridging-zone dynamics in nanocomposites are possible, but this requires novel micromechanical testing methods and detailed analysis that are beyond the scope of the current study.  $^{37-39}$ 

The standard fracture specimens for the results shown in Figure 3 are 3 mm thick, with crack lengths that are larger than the expected R curve. This means that for these large specimens the fracture resistance is independent of the crack length (i.e.,  $R_{\rm ss}^{\rm br}=R^{\rm o}+\Delta R_{\rm ss}^{\rm br}$ ), such that the  $K_{\rm lc}$  values reported in Figure 3 can be properly interpreted as a general property of the material. In contrast to this, solid electrolytes that are employed in batteries are expected to have thicknesses that are less than 1 mm. In these cases, the expected bridging-zone sizes in the rGO nanocomposites (discussed above) will lead to a rising R value that varies significantly over the expected crack length, c. This variation is potentially relevant for the  $\sim$ 700- $\mu$ m-thick specimens employed for the electrochemical measurements in Figure 5, and it is more likely to be a significant factor in the thinner solid electrolytes that are desirable for practical solid-state batteries. The two strain energy-release rate curves in Figure 6B here illustrate the implications of this behavior. Crack extension is first possible at  $G^{\rm o}$ , where the nanocomposite R curve shown corresponds to

$$\left(\frac{dR}{dc}\right)_{c_o} > \left(\frac{dG^{\circ}}{dc}\right)_{c_o}$$
. (Equation 2)





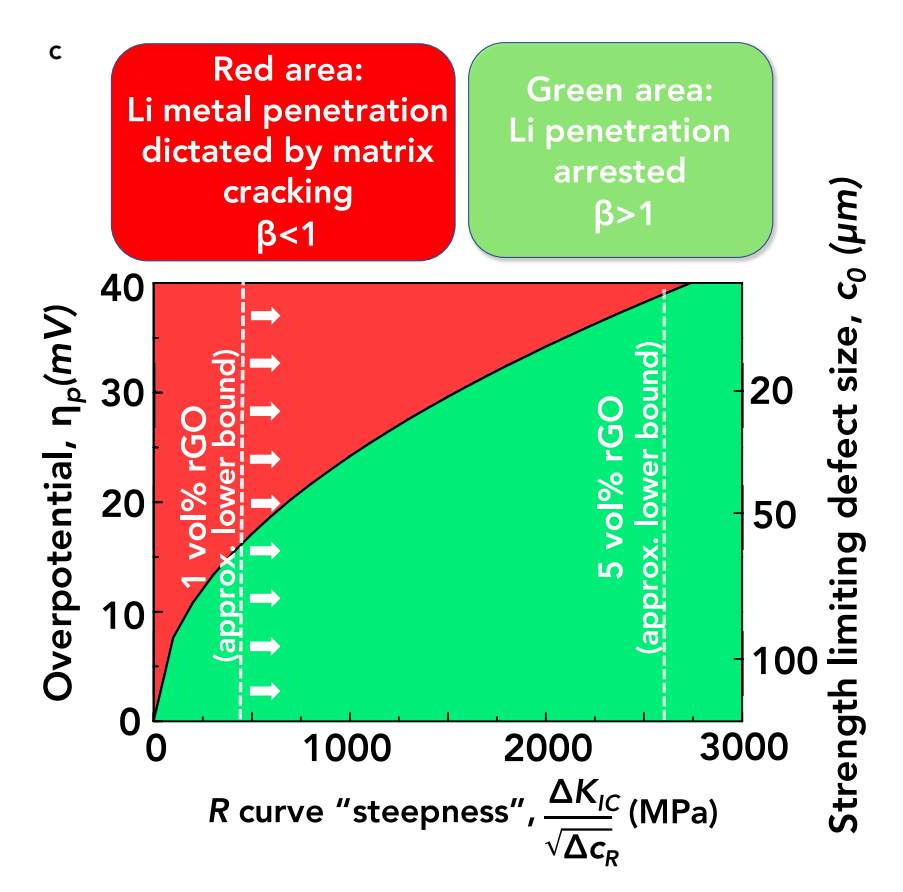


Figure 7. R-Curve Steepness for Preventing Li Metal Penetration in Nanocomposites

(A and B) Simplified schematics of flaws when uniform load  $\sigma_{yy}$  is applied in the electrolyte and of a Li filament in a solid electrolyte matrix. The red arrows depict the applied pressure from the Li metal.

(C) Map based on Equation 18 showing the R-curve "steepness" required to prevent Li-metal penetration. At a given value of the plating overpotential,  $\eta_P$ , the corresponding value of  $c_0$  on the right axis is the limiting flaw size to initiate matrix cracking. The red area ( $\beta$  < 1) shows the regime



#### Figure 7. Continued

where lithium-metal penetration continues to propagate across the electrolyte. The green area ( $\beta$  > 1) corresponds to steeper R curves that will prevent Li metal penetration at this value of  $\eta_P$ . The vertical lines for 1% rGO and 5% rGO are lower bound estimates where the measured values of  $K_{lc}$  are assumed to occur linearly over  $\Delta c_R$  = 100  $\mu$ m. Steeper R curves for these materials are possible (and perhaps likely in our materials), and this will shift these boundaries to the right (as shown by the white arrows).

This condition indicates that crack growth is initially stable, in contrast to the constant  $R^{\circ}$  case described above (matrix only) where the reverse inequality holds. When Equation 2 is valid, crack extension will only occur when the load increases further. The second energy-release rate curve,  $G_{\rm S}(c)$ , corresponds to the highest load where stable crack growth occurs, such that crack extension from  $c_{\rm o}$  to  $c_{\rm s}$  requires an increased load to move from  $G_{\rm o}$  to  $G_{\rm s}$ .

The situation depicted in Figure 6B illustrates that the expected R curves in rGO-reinforced electrolytes should lead to several important effects. First, the full increase in fracture resistance due to the rGO (i.e., the measured  $K_{\rm lc}$  increase in Figure 3) may not be realized (e.g., because the onset of unstable crack growth occurs at  $R_{\rm s}$  in Figure 6B, rather than at  $R_{\rm ss}^{\rm br}$ ). However, this reduction is likely to be modest (e.g., the difference between  $R_{\rm ss}^{\rm br}$  and  $R_{\rm s}$  in Figure 6B). A more important effect is that stable crack extension will occur over length scales that are a significant fraction of the electrolyte thickness.

## **Fracture Toughness Improvements**

A variety of stress states are likely to occur in solid electrolytes, based on different battery architectures, material properties, and external mechanical constraints. With the relatively low  $K_{lc}$  in LATP and other ceramic electrolytes, cracking during handling and cell assembly is one relevant concern. Stresses that can occur during electrochemical cycling introduce additional complexity. These are considered further with the configuration depicted in Figure 5A, with electrode layers that are separated by a thin electrolyte (i.e., similar to a standard coin cell). Tensile stress in the y direction can occur when the Li partial molar volumes are different in the two electrodes, such that moving Li across the cell leads to a net volume change in the stack. For example, if the volume change in the anode exceeds that in the cathode, tensile stress in the electrolyte will occur during discharge. In this state fracture is a possible concern at both of the electrode interfaces and inside the electrolyte. Our present focus is on the bulk properties of the electrolyte, and thus we assume that the interfaces remain strongly bonded at all times. For the simple configuration in Figure 7A, the stress  $\sigma_{vv}^{S}$  will be limited by the softest layer. In metals (e.g., current collectors, Li anodes), the lowest yield stress sets an upper bound, which is quite small with pure Li anodes (<1 MPa). These stresses should not cause electrolyte fracture. Larger stresses can occur with stiffer anodes (e.g., Si or C), but here the yield stress of the current collector can limit the total stress. This suggests an approximate upper bound of  $\sim$ 1 GPa, which roughly corresponds to the yield stress of lithiated Si and some stiff current collectors (e.g., nanocrystalline Ti).

For simplicity, a plane strain analysis is used to consider fracture from the flaws depicted in Figure 7A. With tension acting only in the *y* direction, the mode I stress intensity factor for a sharp internal crack oriented along the *x* direction is given by the following standard expression:<sup>40</sup>

$$K_1 = \psi \sigma_1 \sqrt{c},$$
 (Equation 3)





where  $\sigma_1 = \sigma_{yy}^S$  is the stress applied to the solid electrolyte, c is the crack dimension, and  $\psi$  is a geometric constant with a value of  $\sim$ 1 for this configuration, when  $c/b \ll$ 1. If the R-curve rise in Figure 6B occurs over lengths that are much smaller than c (i.e., such that R is effectively a constant), then the fracture stress is given by

$$\sigma_{\rm f} = \frac{K_{\rm lc}}{\psi \sqrt{c_{\rm f}}},$$
 (Equation 4)

where  $c_f$  is the strength-limiting flaw size. This standard result is applicable to the unreinforced matrix material. For the nanocomposites, Equation 4 is only valid if  $c_f$  is sufficiently large—on the order of hundreds of micrometers or more for the relatively large bridging zones with rGO reinforcements. For these cases the increased  $K_{lc}$ values in Figure 3 indicate that the nanocomposite LATP will increase  $\sigma_f$  by more than a factor of 2 relative to the matrix (assuming that c<sub>f</sub> is the same for both cases). With Li-metal anodes the limiting stress ( $\sigma_{yy}^{S}\sim 1$  MPa) is too small to induce fracture in the matrix or the composite (i.e., this would require  $c_f \sim 1~\mu m$ . For the upper bound stiff electrode/current collector case ( $\sigma_{yy}^{S}\sim 1$  GPa), Equation 4 gives strengthlimiting flaw widths ( $2c_f$ ) of 2.4, 11.4, and 27.2 for the LATP matrix, the 1 vol % rGO, and the 5 vol % rGO composites, respectively. These values are within the range of likely defect populations in thin solid electrolytes, which suggests that volume changes during cycling could lead to fracture if the electrodes and current collectors are relatively stiff. The large decrease in  $c_f$  over this range of  $\sigma_{vv}^S$  values also provides a simple demonstration of the impact that the compliance of the surrounding layers can have on the expected stress and fracture of a ceramic electrolyte during cycling.

For the LATP matrix, Equation 4 provides an appropriate description. However, for the nanocomposite electrolyte studied here, the R-curve considerations introduced in Figure 6B are expected to be relevant. This is certainly the case for the aforementioned small  $c_{\mathrm{f}}$  values obtained with the  $\sigma_{yy}^{\mathrm{S}}$  upper bound. In general, the strength-limiting flaw sizes in solid electrolytes will be smaller than the expected solid electrolyte thicknesses of  $\sim 100 \mu m$ , such that crack extension will occur over distances where significant R-curve effects are expected in the rGO-reinforced composites. For these flaw sizes LSB effects in the nanocomposites will lead to stable crack growth (e.g., from  $c_o$  to  $c_s$  in Figure 6B). In contrast, unstable crack growth (i.e., brittle fracture) will occur for the matrix material (under the same loading conditions). This comparison is shown schematically in Figure 6B. The damage-tolerant behavior with the composite can then lead to a ductile response after the onset of matrix cracking. This should resemble failure mechanisms that occur in large fiber ceramic matrix composites.

For uniaxial tensile stress in the x direction, it is convenient to consider the flaw at the electrolyte/anode interface. For the matrix-only case, fracture here can again be described with Equation 4, which leads to only a slight difference in the value of  $\sigma_f$  for a given  $c_f$  (compared with crack extension from the internal flaw). Based on the expected electrolyte thicknesses, LSB effects will invariably impact crack extension in the y direction for the rGO-reinforced nanocomposites. One important implication is that stable crack growth along the curve can potentially allow the propagation of multiple cracks, in contrast to the formation of one catastrophic through-thickness crack that will occur with the conventional brittle fracture that is expected in the single-phase LATP material. This damage-tolerant response in the nanocomposites can provide additional benefits beyond just the increase in the measured  $K_{lc}$  values in Figure 3.



#### **Lithium-Metal Penetration**

Recent studies have also proposed that Li-filled flaws can create relatively high stress inside of the solid electrolyte, as shown in Figure 7B.  $^{41-44}$  A flaw that is initially empty should fill with Li during plating. Using a completely filled flaw with no stress as a logical initial state, current focusing at the tip will then lead to a rapid stress buildup inside of the flaw. In the limit where Li atoms are immobile, the Li can reach a limiting hydrostatic stress,  $\widehat{\sigma}_p^{\text{max}}$ . This is defined as the value that exactly counteracts the local overpotential,  $\eta_P$ , such that  $\Delta \Gamma_{\text{Li}} = 0 = \mathcal{F} \eta_P - V_{\text{m}}^{\text{Li}} \widehat{\sigma}_P$ , which leads to

$$\widehat{\sigma}_{P}^{\text{max}} = \frac{\mathcal{F} \, \eta_{P}}{V_{\text{Li}}^{\text{Li}}},$$
 (Equation 5)

where  $\mathcal{F}$  is Faraday's constant and  $V_{\rm m}^{\rm Li}$  is the molar volume of Li. For this limiting case where there is no relaxation of the internal stress, the Li flux into the flaw ceases when the stress in the flaw reaches,  $\widehat{\sigma}_{\rm P}^{\rm max}$ . This static state should occur relatively quickly. Note that away from the flaw, there is still a Li ion flux between the planar Li-metal interfaces (i.e., a steady-state flux under galvanostatic conditions).

The stress in Equation 5 provides a convenient limiting case for describing the conditions where internal mechanical forces lead to the extension of a Li-filled flaw. The quantity  $\mathcal{F}/V_m^{\text{Li}}$  is 7.4 MPa mV<sup>-1</sup>,<sup>45</sup> which clearly shows that relatively small overpotentials can lead to large internal compressive stress. Based on standard linear elastic fracture mechanics, this type of internal force in the Li corresponds to a mode I stress intensity factor at the tip of a narrow, straight flaw that is given by

$$K_1 = 2\sqrt{\frac{c}{\pi}} \int_0^c \frac{\sigma_{xx}^{flaw}(y)}{\sqrt{c^2 - y^2}} dy,$$
 (Equation 6)

where  $\sigma_{xx}^{flaw}(y)$  is the normal force acting on the flaw faces. Fracture of the solid electrolyte should occur when this value exceeds the fracture toughness (i.e.,  $K_l > K_{lc}$ ). To better understand this behavior, it is convenient to note that with a constant value of  $\sigma_{xx}^{flaw} = \widehat{\sigma}_P^{max}$ , Equation 6 is identical to the result obtained for standard mode I brittle fracture with a fixed external load equal to  $\widehat{\sigma}_P^{max}$  (i.e., Equation 3 with  $\psi \sim$  1). However, it is important to note that the internal stress acting here ( $\sigma_{xx}^{flaw}$ ) is different from the external loading configuration. In both cases, the driving force for crack extension can be described with the energy-release rate. This quantity is given here by

$$G = -\left(\frac{dU_E}{dc} + \frac{dU_F}{dc}\right),$$
 (Equation 7)

where  $U_{\rm E}$  is the stored elastic strain energy in the solid electrolyte. The second term,  $dU_{\rm F}/dc$ , describes the energy-release rate in the Li-filled filament. The general criterion for Li penetration is then

$$G \ge R$$
, (Equation 8)

where *R* is the fracture resistance of the solid electrolyte. With stiff ceramic electrolytes, it is likely that *G* is dominated by the first term in Equation 7. For mode I loading this gives the same result for both the externally and internally loaded configurations:

$$G_{\rm E} = \frac{dU_{\rm E}}{dc} = \frac{K_{\rm I}^2}{E_E'}$$
 (Equation 9)

Although these expressions are identical for the two cases, with the internal force applied by the Li metal it is expected that

$$\frac{dG_{\rm E}}{dc} < 0. (Equation 10)$$





The opposite occurs when the load is applied externally (e.g., the increase in G with c that is shown in Figure 6B). With this decrease in the driving force ( $G_E$ ) as c increases, stable crack extension will occur. As noted in Figure 6B, unstable crack growth corresponds to brittle fracture with a crack that extends across the electrolyte almost instantaneously. However, for configurations where the stability criterion in Equation 10 is met, additional crack extension only occurs when the load is increased. The Li-metal penetration case is somewhat different. For the basic treatment presented here, it is assumed that stable crack extension first opens space at the tip, such that  $K_{lc}$  values are an appropriate measure of the fracture resistance. Immediately following this incremental increase in c, the internal pressure forces Li into this space. This crack extension process will decrease the internal pressure and lead to the decrease in  $G_E$  that is shown in Equation 10. This will continue if the net flux of Li into the flaw increases the internal pressure back to the level required for stressdriven crack extension (i.e., by counteracting the stress drop associated with the increase in c). With this in mind, the general extension of a Li-filled filament should correspond to a Li flux that coincides with the following steady-state condition:

$$\frac{dG_{\rm E}}{dc} = \frac{dR}{dc}.$$
 (Equation 11)

This condition means that the filament extension criterion ( $G_E = R$ ) is maintained as cincreases. For example, if this is applied to the constant R case, the Li flux into the growing flaw must maintain a constant energy-release rate. The relationship between  $dG_F/dc$  and the net flux of Li into the flaw is complex, and detailed modeling can be used to assess specific mechanisms. The simplified case where the stress in the flaw is constant can be used to provide some basic insight.

It is first convenient to assess the behavior of a brittle elastic material with a constant fracture resistance, Ro (i.e., a monolithic ceramic electrolyte such as LATP). Here, the basic fracture requirement is

$$G_{\rm E} = \frac{dU_{\rm E}}{dc} = \frac{\pi c}{E_{\rm E}'} \hat{\sigma}_{\rm c}^2 = R^{\circ}.$$
 (Equation 12)

For this case, Equation 11 becomes

$$\frac{dG_{\rm E}}{dc} = \frac{\pi}{E_{\rm E}'} \hat{\sigma}_{\rm c} \left[ \hat{\sigma}_{\rm c} + 2c \frac{d\hat{\sigma}_{\rm c}}{dc} \right] = 0.$$
 (Equation 13)

Solving Equations 12 and 13 for an initial condition,  $\sigma(c_o) = \sigma_o$ , then gives

$$\widehat{\sigma}_{c} = \widehat{\sigma}_{o} \sqrt{\frac{c_{o}}{c}} = \sqrt{\frac{E'_{E} R^{o}}{\pi c}}$$
 (Equation 14)

This result indicates that  $\hat{\sigma}_{c}$ , the internal stress required to propagate the Li-filled flaw, will decrease as c increases. The basic model outlined above leads to two significant predictions:

- Based on the stability condition in Equation 10, Li-filled flaws will move through the electrolyte at an observable rate dictated by Equation 11 (in contrast to unstable crack propagation, which generally occurs too quickly to be directly observed).
- If the plating potential is fixed, a Li filament that begins to penetrate through the electrolyte will continue to propagate.

The first statement is fully consistent with in situ microscopy, which shows that Li-filled flaws can be observed as they move through the electrolyte. 41-44 The



second statement is based on Equation 14, where it is seen that the stress required for crack extension,  $\hat{\sigma}_c$ , decreases with increasing crack length. This indicates that to halt the propagation of this crack during plating, the driving force for stress build up (i.e., the plating potential  $\eta_P$ ) must be decreased.

For the nanocomposite electrolytes, a rising R curve can prevent the continuing Li-filament propagation that is described above. A simple model can be obtained for a constantly increasing R value,  $\rho = dR/dc$  (this quantity is an estimate of the initial increase above  $R^{\circ}$  that is depicted in Figure 6B). Inserting this into Equation 14 gives

$$\widehat{\sigma}_{c}\left[\widehat{\sigma}_{c} + 2c \frac{d\widehat{\sigma}_{c}}{dc}\right] = \frac{E_{E}'\rho}{\pi}.$$
 (Equation 15)

If one again considers the limiting case where  $\sigma_{yy}^{\text{flaw}}$  along the flaw is constant, Equation 15 can be solved (with constant  $\rho$  and the initial condition,  $\sigma(c_{\text{o}}) = \sigma_{\text{o}}$ ), to give

$$\left(\frac{\widehat{\sigma}_c}{\sigma_o}\right)^2 = \beta + (1 - \beta) \frac{c_o}{c},$$
 (Equation 16)

where  $\beta=(E_E'\rho)/(\pi\,\sigma_o^2)$ . For constant  $R^o$  (i.e.,  $\beta=0$ ), this result reduces to Equation 14 as expected. A rising R curve corresponds to  $\beta>0$ . Based on Equation 16,  $\beta>1$  leads to

$$\frac{d\hat{\sigma}_c}{dc}$$
>1. (Equation 17)

When this condition holds, it means that the continuing filament extension into the electrolyte that is implied by Equation 15 will not occur (i.e., because the stress needed to propagate the filament,  $\widehat{\sigma}_{\rm c}$ , increases). For the LATP nanocomposites,  $\beta$  can be estimated from measured quantities. The value of  $\sigma_{\rm o}$  is viewed as the threshold for initial matrix cracking, which can be evaluated with Equation 4 to give

$$\beta = \frac{E_{\rm E}' \rho}{\pi \sigma_{\rm o}^2} \sim \frac{\psi^2}{\pi} \left(\frac{\Delta K_{\rm lc}}{K_{\rm lc}^{\rm o}}\right)^2 \frac{c_{\rm o}}{\Delta c_{\rm R}}.$$
 (Equation 18)

Here,  $\rho \sim \Delta R/\Delta c_R$  is a rough linear approximation of the R curve that can be interpreted with the increase in fracture toughness,  $\Delta K_{lc}$ , over a bridging zone of size  $\Delta c_R$ .

A map showing the implications of Equation 18 is shown in Figure 7C. The solid boundary here corresponds to  $\beta=1$ . At a fixed  $\eta_P$  (the local overpotential),  $c_o$  is the lower bound on the limiting size of a Li-filled flaw that satisfies the fracture criteria for the matrix (defined by Equations 4 and 5, with  $c_f=c_o$ ,  $K_{lc}=K_{lc}^o$ , and  $\sigma_f=\widehat{\sigma}_P^{max}$ ). When a limiting flaw of size  $c_o$  is subjected to an overpotential that initiates matrix cracking, the flaw is expected to propagate through the electrolyte if  $\beta<1$  (at fixed  $\eta_P$ ). Li-metal penetration will be blocked if  $\beta>1$ . This assessment reflects the expectation that a steeper R curve is needed to halt Li-metal penetration after it begins. The lower bound estimates for the 1% and 5% nanocomposites are based on material where the measured toughness increase in Figure 3 is spread over 100  $\mu$ m, which is the lower bound of values measured in rGO-reinforced ceramics. <sup>11</sup> A bridging zone that evolves over shorter lengths is also feasible, and thus the range shown here provides rough lower estimates. This simplified model predicts that a steeper R curve due to higher toughness or shorter  $\Delta c_R$  can substantially increase the range of conditions where Li penetration will be blocked. Overall, this framework provides





important guidelines for the design and development of future nanocomposite solid electrolytes that are expected to have thicknesses on the order of 100  $\mu m$  or less.

#### **Conclusions**

Fracture toughness is a crucial parameter that is expected to have a major impact on battery cell performance with SSEs. Increasing the toughness of single-phase ceramic solid electrolytes is likely to be limited to relatively modest improvements at best, and thus nanocomposites can enable more substantial toughening. This is demonstrated in the work reported here, where reinforcing a ceramic solid electrolyte with small amounts of rGO produced significant increases in fracture toughness, with minimal changes in the ionic conductivity. The more than two-fold increase in the toughness of LATP results in the highest K<sub>Ic</sub> yet reported for an inorganic solid electrolyte, and an analysis of the chemo-mechanical behavior of these materials leads to guidelines for designing toughened electrolytes that can resist Li-metal penetration. This work also provides impetus for exploring other nanoscale reinforcements that can improve the performance of ceramic solid electrolytes.

## **EXPERIMENTAL PROCEDURES**

## Resource availability

All data are available upon reasonable request.

#### Lead Contact

B.W. Sheldon serves as lead contact and is familiar with the Cell Press editorial policies.

## Materials Availability

In this study, no new unique reagents were generated.

## **Material Processing and Structural Characterization**

LATP composite specimens were prepared by SPS. This method utilizes the combination of uniaxial force and pulsed direct electrical current in a controlled atmosphere to perform rapid consolidation of powders. The use of direct electrical current allows very high heating rates (1,000°C min<sup>-1</sup>), roughly an order of magnitude greater than that in conventional sintering techniques. This results in fine-grained microstructure and high densities. 11-14 The LATP source material was nanopowder (NEI, Somerset, NJ, USA). For the composites, this was combined with GO and dispersed in ethanol by sonication (1 h). The GO powder was prepared using the modified Hummers' method, which entails chemical exfoliation of graphite.<sup>46</sup> In brief, graphene flakes were chemically exfoliated in a mixture of P<sub>2</sub>O<sub>5</sub> and K<sub>2</sub>S<sub>2</sub>O<sub>8</sub> in concentrated H<sub>2</sub>SO<sub>4</sub> at 80°C for 4.5 h. The resulting product was washed with deionized water repeatedly until neutral pH was achieved. The solution was then dried and mixed in a solution of KMnO<sub>4</sub>, H<sub>2</sub>O<sub>2</sub>, and H<sub>2</sub>SO<sub>4</sub> to achieve complete exfoliation and functionalization of the graphene layers into GO. Finally, the GO powder was centrifuged, freeze-dried, and dispersed in ethanol (1 h). The mixture was stirred for 30 min and dried on a hotplate. The mixed dry powders of LATP and graphene oxide were crushed in an agate mortar to eliminate any agglomerates, and SPS'd (Thermal Technologies, Santa Rosa, CA, USA) at 950°C, with a dwell time of 5 min and 75 MPa of pressure in an Ar atmosphere, resulting in LATP with 1 vol % or 5 vol % rGO. All the SPSed pellets were mechanically ground to remove any extraneous surface layers from the SPS process.

The density of the LATP and the LATP/rGO materials was measured using the Archimedes principle, with deionized water as the immersion medium. The rule of



mixtures was used to calculate the theoretical density of the nanocomposite with 1 vol % (2.91 mg  $m^{-3}$ ) and 5 vol % (2.88 mg  $m^{-3}$ ) of rGO, respectively, using the following densities of the pure phases: LATP (2.92 mg  $m^{-3}$ )<sup>16,17</sup> and rGO (2.2 mg m<sup>-3</sup>). Regarding the latter, there are no reports on accurate density measurement of rGO, and therefore, the bulk density of graphite is used to estimate the theoretical density of the nanocomposite. Fracture surfaces of the LATP and LATP nanocomposites were observed by a scanning electron microscope (LEO 1530VP, Carl Zeiss, Germany) operated at 10 kV accelerating voltage. The intercept method was used to determine the average grain size based on SEM images obtained at 20 different locations of the material. For the density measurements, rectangular specimens of 1 mm width, 1 mm thickness, and 20 mm length were cut from the center of the SPSed pellets. No significant variation in the grain size was observed across the thickness or diameter of these specimens. Based on SEM observations, the rGO reinforcements align normally to the SPS pressing direction. Structural characterization was conducted using XRD (D8 High-resolution X-ray Diffractometer, Bruker, Billerica, MA, USA) at a scan rate of 4 min<sup>-1</sup> and Raman spectroscopy (Alpha 300 M+, WITec, Germany) with 532 nm irradiation. The Raman scans were obtained with an integration time of 50 ms per spectrum.

## **Fracture Toughness Characterization**

Two different methods were employed to measure the fracture toughness of the monolithic LATP and the composites (LATP with 1 vol % or 5 vol % rGO). Vickers indentation with a load of 2 N was used for monolithic LATP. The elastic modulus, E, and, hardness, H, were measured using nanoindentation (Bruker) at 20 different locations of the material's polished surface (1 µm finish) using a load of 1.5 mN.<sup>47</sup> The elastic modulus was determined by using the Oliver-Pharr method, 48 while the hardness was as per the ASTM C1327 standard.<sup>49</sup> The length of the cracks was measured by SEM. However, nanoindentation only provides accurate values for single-phase materials.<sup>24,25</sup> Therefore, for the composites, toughness was measured according to the ASTM C1421 standard, 50 where a single-edge-notched beam is used. These specimens were machined (5 mm width, 5 mm thickness, 20 mm length), and a sharp notch was introduced using a Knoop indenter and a load of 5 N. The initial crack depth and width were measured accurately using an optical microscope after the failure of each specimen. Fracture tests were conducted in three-point bending using displacement control in a universal testing machine (Instron 5800, Norwood, MA, USA).

## **Electrochemical Measurements**

For electrochemical measurements, a 100-nm gold film (blocking electrode) was deposited on both sides of the solid electrolyte using e-beam deposition (Kurt J. Lesker, Lab 18, Jefferson Hills, PA, USA). Coin cells (2032 type) with spacers and springs were prepared in an argon-filled glovebox. Additional PEO-coated electrolyte for cycling experiments was prepared by dissolving PEO (MW: 700,000 g mol $^{-1}$ ) and tetraglyme (MW: 222.28 g mol $^{-1}$ ) with LiTFSI in ethanol/deionized water (1:1). This was applied on both sides of the solid electrolyte, and symmetric cells were then assembled with 600-µm-thick Li metal for both electrodes. Cycling was performed by applying constant currents of 0.01 mA cm $^{-2}$  for 8-h cycles. This corresponds to plating and stripping of 0.4 µm of Li after each cycle.

For ionic conductivity measurements, AC impedance spectra were obtained under open-circuit conditions at room temperature using a potentiostat (VMP-3, Biologic Science Instruments, Grenoble, France). The frequency ranged from 0.01 Hz to 1 MHz, and the applied voltage amplitude was 40 mV. The diameter of the





impedance semicircle corresponds to the grain and grain-boundary resistance of the LATP electrolyte. The Li-ion conductivities of the LATP electrolyte were obtained using the following relation:<sup>51</sup>

$$\sigma(\Omega.\text{cm})^{-1} = t/R_bA,$$
 (Equation 19)

where  $\sigma$  is the ionic conductivity,  $R_{\rm b}$  is the bulk resistance, t is the thickness of the electrolyte, and A is the area of the deposited gold blocking electrodes. The electronic conductivity was measured under DC polarization at 100 mV. At a constant voltage, the current first decreases and then reaches a steady-state value, which is attributed to electronic leakage.<sup>51</sup>

#### **ACKNOWLEDGMENTS**

C.E.A., C.R., N.P.P., and B.W.S. gratefully acknowledge financial support from the US Department of Energy, Office of Basic Energy Science, through award number DE-SC0018113 (J. Vetrano, Program Manager). M.Y.J. and B.W.S. also acknowledge support from the National Science Foundation, Ceramics Program (DMR-1832829).

#### **AUTHOR CONTRIBUTIONS**

C.E.A. and C.R. designed the project. C.E.A. prepared the electrolyte materials and performed mechanical characterization experiments. M.Y.J. performed the electrochemical characterization. C.E.A. and B.W.S. developed the analytical model. C.E.A., M.Y.J., and B.W.S. wrote the manuscript. B.W.S. and N.P.P. guided the project. All authors contributed to the data analysis.

## **DECLARATION OF INTERESTS**

The authors declare no competing interests.

Received: December 26, 2019 Revised: April 11, 2020 Accepted: May 5, 2020

Published: June 5, 2020

## **REFERENCES**

- 1. Nitta, N., Wu, F., Lee, J.T., and Yushin, G. (2015). Li-ion battery materials: present and future. Mater. Today 18, 252–264.
- 2. Tarascon, J.-M., and Armand, M. (2001). Issues and challenges facing rechargeable lithium batteries. Nature 414, 359-367
- 3. Armand, M., and Tarascon, J.-M. (2008). Building better batteries. Nature 451, 652-657.
- 4. Hao, F., Chi, X., Liang, Y., Zhang, Y., Xu, R., Guo, H., Terlier, T., Dong, H., Zhao, K., Lou, J. and Yao, Y. (2019). Taming active material-solid electrolyte interfaces with organic cathode for all-solid-state batteries. Joule 3, 1349–1359.
- 5. Wan, J., Xie, J., Mackanic, D.G., Burke, W., Bao, Z., and Cui, Y. (2018). Status, promises, and challenges of nanocomposite solid-state electrolytes for safe and high performance lithium batteries. Mater. Today Nano 4, 1–16.
- 6. Fu, W., Zhao, E., Sun, Z., Ren, X., Magasinski, A., and Yushin, G. (2018). Iron fluoride-carbon nanocomposite nanofibers as free-standing cathodes for high-energy lithium batteries. Adv. Funct. Mater. 28, 1801711.

- 7. Yan, G., Yu, S., Yang, W., Li, X., Tempel, H., Kungl, H., Eichel, R.-A., Kruger, M., and Malzbendder, J. (2019). Anisotropy of the mechanical properties of Li<sub>1.3</sub>Al<sub>0.3</sub>Ti<sub>1.7</sub>(PO<sub>4</sub>)<sub>3</sub> solid electrolyte material. J. Power Sources
- 8. Kim, Y., Jo, H., Allen, J.L., Choe, H., Wolfenstine, J., and Sakamoto, J. (2016). The effect of relative density on the mechanical properties of hot-pressed cubic Li<sub>7</sub>La<sub>3</sub>Zr<sub>2</sub>O<sub>12</sub>. J. Am. Ceram. Soc. 99, 1367-1374.
- 9. Wolfenstine, J., Allen, J.L., Sakamoto, J., Siegel, D.J., and Choe, H. (2018). Mechanical behavior of Li-ion conducting crystalline oxidebased solid electrolytes: a brief review. Ionics 24, 1271-1276.
- 10. Yang, Y., Liang, X., Chen, W., Cao, L., Li, M., Sheldon, B.W., and Lou, J. (2015). Quantification and promotion of interfacial interactions between carbon nanotubes and polymer derived ceramics. Carbon 95, 964-971
- 11. Wang, Q., Ramirez, C., Watts, C.S., Borrero-Lopez, O., Ortiz, A.L., Sheldon, B.W., and

- Padture, N.P. (2019). Fracture, fatigue, and sliding-wear behavior of nanocomposites of alumina and reduced graphene-oxide. Acta Mater. 186, 29-39.
- 12. Ramirez, C., Wang, Q., Belmonte, M., Miranzo, P., Osendi, M.I., Sheldon, B.W., and Padture, N.P. (2018). Direct in situ observation of toughening mechanisms in nanocomposites of silicon nitride and reduced graphene-oxide. Scripta Mater. 149, 40-43.
- 13. Curtin, W.A., and Sheldon, B.W. (2004). CNTreinforced ceramics and metals. Mater. Today 7. 44-49.
- 14. Walker, L.S., Marotto, V.R., Rafiee, M.A., Koratkar, N., and Corral, E.L. (2011). Toughening in graphene ceramic composites. ACS Nano 5, 3182–3190.
- 15. Dewees, R., and Wang, H. (2019). Synthesis and properties of NaSICON-type LATP and LAGP solid electrolytes. ChemSUSChem 12, 3713-
- 16. Zhu, H., and Liu, J. (2018). Emerging applications of spark plasma sintering in all

## **Matter**

## Article



- solid-state lithium-ion batteries and beyond. J. Power Sources 391, 10–25.
- Kali, R., and Mukhopadhyay, A. (2014). Spark plasma sintered/synthesized dense and nanostructured materials for solid-state Li-ion batteries: overview. J. Power Sources 247, 920–931.
- Palmero, P. (2015). Structural ceramic nanocomposites: a review of properties and powders' synthesis methods. Nanomaterials 6, 656-696.
- Narvaez-Semanate, J.L., and Rodrigues, A.C.M. (2010). Microstructure and ionic conductivity Li<sub>1+x</sub>Al<sub>x</sub>Ti<sub>2-x</sub>(PO<sub>4</sub>)<sub>3</sub> NASICON glass-ceramics. Solid State Ion. 181, 1197– 1204.
- Gong, Y., Fu, K., Xu, S., Dai, J., Hamann, T.R., Zhang, L., Hitz, G.T., Fu, Z., Ma, Z., McOwen, D.W., et al. (2018). Lithium-ion conductive ceramic textile: a new architecture for flexible solid-state lithium metal batteries. Mater. Today 21, 594–601.
- Xu, S., McOwen, D.W., Wang, C., Zhang, L., Luo, W., Chen, C., Li, Y., Gong, Y., Dai, J., Kuang, Y., et al. (2018). Three-dimensional, solid-state mixed electron-ion conductive framework for lithium metal anode. Nano Lett. 18, 3926–3933.
- Duluard, S., Paillassa, A., Puech, L., Vinatier, P., Turq, V., Rozier, P., Lenormand, P., Taberna, P.L., Simon, P., and Ansart, F. (2013). Lithium conducting solid electrolyte Li<sub>1.3</sub>Al<sub>0.3</sub>Ti<sub>1.7</sub>(PO<sub>4</sub>)<sub>3</sub> obtained via solution chemistry. J. Eur. Ceram. Soc. 33, 1145–1153.
- Ferrari, A., and Basko, D.M. (2013). Raman spectroscopy as a versatile tool for studying the properties of graphene. Nat. Nanotech. 8, 235–246.
- Sheldon, B.W., and Curtin, W.A. (2004). Nanoceramic composites: tough to test. Nat. Mater. 3, 505–506.
- Wang, X., Padture, N.P., and Tanaka, H. (2004). Contact-damage-resistant ceramic/single-wall carbon nanotubes and ceramic/graphite composites. Nat. Mater. 3, 539–544.
- Wu, J.-F., and Guo, X. (2017). Origin of the low grain boundary conductivity in lithium ion conducting perovskites: Li<sub>3x</sub>La<sub>0.67-x</sub>TiO<sub>3</sub>. J. Chem. Phys. 8, 5880–5887.
- Liu, K., Li, Y., Zhang, R., Wu, M., Huang, B., and Zhao, T. (2019). Facile surface modification method to achieve an ultralow resistance in garnet-based Li metal batteries. ACS Appl. Energy Mater. 2, 6332–6340.
- 28. Chen, R.J., Huang, M., Huang, W.Z., Shen, Y., Lin, Y.H., and Nan, C.W. (2014). Effect of

- calcining and AI doping on structure and conductivity of Li<sub>7</sub>La<sub>3</sub>Zr<sub>2</sub>O<sub>12</sub>. Solid State Ion. 265, 7–12.
- Wolfenstine, J., Rangasamy, E., Allen, J.L., and Sakamoto, J. (2012). High conductivity of dense tetragonal Li<sub>7</sub>La<sub>3</sub>Zr<sub>2</sub>O<sub>12</sub>. J. Power Sources 208, 193–196.
- Zhu, Y., He, X., and Mo, Y. (2015). Origin of outstanding stability in the lithium solid electrolyte materials: insights from thermodynamic analyses based on first principles calculations. ACS Appl. Mater. Interfaces 7, 23685.
- Sharafi, A., Meyer, H.M., Nanda, J., Wolfenstine, J., and Sakamoto, J. (2016). Characterizing the Li-Li<sub>7</sub>La<sub>3</sub>Zr<sub>2</sub>O<sub>12</sub> interface stability and kinetics as a function of temperature and current density. J. Power Sources 302, 1335–1339.
- Van den Broek, J., Afyon, S., and Rupp, J.L.M. (2016). Interface-engineered all-solid-state Liion batteries based on garnet-type fast Li<sup>+</sup> conductors. Adv. Energy Mater. 6, 1600736.
- 33. Han, F., Westover, A.S., Yue, J., Fan, X., Wang, F., Chi, M., Leonard, D.N., Dudney, N.J., Wang, H., and Wang, C. (2019). High electronic conductivity as the origin of lithium dendrite formation within solid electrolytes. Nat. Energy. 4, 187–196.
- Cheng, Q., Li, A., Li, N., Li, S., Zangiabadi, A., Li, T.D., Huang, W., Li, A.C., Jin, T., Song, Q., et al. (2019). Stabilizing solid electrolyte-anode interface in Li-metal batteries by boron nitridebased nanocomposite coating. Joule 3, 1510– 1522.
- Bao, G., and Suo, Z. (1992). Remarks on crackbridging concepts. Appl. Mech. Rev. 45, 355–366.
- Lin, D., Liu, C.R., and Cheng, G.J. (2014). Single-layer graphene oxide reinforced metal matrix composites by laser sintering: microstructure and mechanical property enhancement. Acta Mater. 80, 183–193.
- Athanasiou, C.E., Zhang, H., Ramirez, C., Xi, J., Baba, T., Wang, X., Zhang, W., Padture, N.P., Szlufarska, I., and Sheldon, B.W. (2020). High toughness carbon-nanotube-reinforced ceramics via ion-beam engineering of interfaces. Carbon 163, 169–177.
- 38. Liu, X., Athanasiou, C.E., Padture, N.P., Sheldon, B.W., and Gao, H. (2020). A machine learning approach to fracture mechanics problems. Acta Mater. 190, 105–112.
- Athanasiou, C.E., and Bellouard, Y. (2015). A monolithic micro-tensile tester for investigating silicon dioxide polymorph

- micromechanics, fabricated and operated using a femtosecond laser. Micromachines 6, 1365–1386.
- 40. Lawn, B. (1993). Fracture of Brittle Solids, Second Edition (Cambridge University Press).
- Klinsmann, M., Hildebrand, F.E., Ganser, M., and McMeeking, R.M. (2019). Dendritic cracking in solid electrolytes driven by lithium insertion. J. Power Sources 442, 22722.
- 42. Porz, L., Swamy, T., Sheldon, B.W., Rettenwander, D., Fromling, T., Thaman, H.L., Berendts, S., Uecker, R., Carter, W.C., and Chiang, Y.-M. (2017). Mechanism of lithium metal penetration through inorganic solid electrolytes. Adv. Energy Mater. 7, 1701003.
- 43. Swamy, T., Park, R., Sheldon, B.W., Rettenwander, D., Porz, L., Berendts, S., Uecker, R., Carter, W.C., and Chiang, Y.-M. (2018). Lithium metal penetration induced by electrodeposition through solid electrolytes: example in single-crystal Li<sub>b</sub>La<sub>3</sub>ZrTaO<sub>12</sub> garnet. J. Electrochem. Soc. 165, 3648–3655.
- 44. McGrogan, F.P., Swamy, T., Bishop, S.R., Eggleton, E., Porz, L., Chen, X., Chiang, Y.-M., and Van Vliet, K.J. (2017). Compliant yet brittle mechanical behavior of Li<sub>2</sub>S-P<sub>2</sub>S<sub>5</sub> lithium-ionconducting solid electrolyte. Adv. Energy Mater. 7, 1602011.
- Bishop, S.R., Perry, N., Marrocchelli, D., and Sheldon, B. (2017). Electro-Chemo-Mechanics of Solids (Springer International Publishing).
- Zaaba, N.I. (2017). Synthesis of graphene oxide using modified hummers method: solvent influence. Proced. Eng. 184, 469–477.
- Anstis, G.R., Chantikul, P., Lawn, B.R., and Marshall, D.B. (1981). A critical evaluation of indentation techniques for measuring fracture toughness: I, direct crack measurements. J. Am. Ceram. Soc. 64, 533–538.
- Oliver, W.C., and Pharr, G.M. (1992). An improved technique for determining hardness and elastic modulus using load and displacement sensing indentation experiments. J. Mar. Res. 7, 1564–1583.
- ASTM C1327-15, Standard Test Method for Vickers Indentation Hardness of Advanced Ceramics. ASTM International, West Conshohocken, PA, 2018, www.astm.org.
- ASTM C1421 18, Standard Test Methods for Determination of Fracture Toughness of Advanced Ceramics at Ambient Temperature. ASTM International, West Conshohocken, PA, 2018, www.astm.org.
- Bruce Wagner, J., and Wagner, C. (1957). Electrical conductivity measurements on cuprous halides. J. Chem. Phys. 26, 1597–1601.